Extreme Mechanics Letters 29 (2019) 100449

Contents lists available at ScienceDirect

Extreme Mechanics Letters

journal homepage: www.elsevier.com/locate/eml

An analytical model for the design of Peano-HASEL actuators with drastically improved performance

Nicholas Kellaris [a,b], Vidyacharan Gopaluni Venkata [a], Philipp Rothemund [a], Christoph Keplinger [a,b,*]

[a] Department of Mechanical Engineering, University of Colorado, Boulder, CO 80309, USA
[b] Materials Science and Engineering Program, University of Colorado, Boulder, CO 80303, USA

ARTICLE INFO

Article history:
Received 7 February 2019
Received in revised form 21 March 2019
Accepted 22 March 2019
Available online 29 March 2019

Keywords:
Soft robotics
Artificial muscles
Electroactive polymers
Peano-HASEL actuators

ABSTRACT

The emerging field of soft robotics promises applications in areas such as human–machine interaction, industrial automation, and biomedical devices. Electrohydraulic Peano-HASEL (hydraulically amplified self-healing electrostatic) actuators feature muscle-like linear contraction on activation, fast operation, and direct electrical control, which makes them a versatile actuator for soft robotics. To better understand the impact of geometry and materials on actuator performance, we develop an analytical model – based on minimizing the total energy of the actuator system – that accurately predicts the quasi-static behavior of the actuators without relying on fitting parameters. We present extensive experimental validation of this model for actuators with varying geometries, as well as actuators made from shell materials with different electrical and mechanical properties. Using these results, we identify design rules for the development of actuators with tunable force-strain characteristics. As a key result of this paper, we lay out a roadmap for creating Peano-HASELs with drastically improved specific energies. Specifically, we identify a combination of pouch geometry and an existing high-performance shell material for which the model predicts actuators that achieve a specific energy of over 10,000 J/kg, far exceeding maximum values reported for natural muscle (∼ 40 J/kg).

1. Introduction

Linear actuators are an enabling technology in areas such as industrial automation, automobiles, robotics, and aerospace. Traditional linear actuators – typically made from electric motors and gears – are noncompliant, complex, and bulky, which limits their adaptability and increases the risk of injury during human–robot interactions in collaborative environments [1,2]. To address these issues, there have been efforts to design actuators from soft, compliant materials for use in soft robotic systems [3–12].

Electrohydraulic HASEL (hydraulically amplified self-healing electrostatic) actuators are a new class of soft actuators that use electrostatic forces to drive shape change in a soft hydraulic structure. HASELs have shown promise as soft actuators for robotic systems [13,14], as they combine the speed, efficiency, and electrical control of dielectric elastomer actuators (DEAs) [15–20], with the versatility of soft fluidic actuators [21–23]. A subset of these actuators – called Peano-HASEL actuators – have been demonstrated as fast and versatile muscle-like actuators that linearly contract on activation without the use of rigid frames or prestretch [14]; in contrast to DEAs, Peano-HASELs can use flexible, rather than stretchable, materials for the actuator structure and electrodes. As such, they can be fabricated with a variety of materials using industrially-compatible fabrication methods. To date, Peano-HASELs have demonstrated 10% linear contraction, a bandwidth up to 50 Hz, the ability to scale up actuation force, and versatility in materials design [14]. Moving forward, a theory-driven approach to designing Peano-HASELs will help elucidate current actuation characteristics and enable the design of actuators with improved performance.

In this work, we derive an analytical model for the quasi-static behavior of Peano-HASEL actuators that does not rely on fitting parameters. We validate the model experimentally for different actuator geometries and materials and find robust agreement between the predicted and the observed behavior. Based on the model, we investigate the influence of geometry and material parameters on the actuation force, actuation strain, and energy density of Peano-HASEL actuators. In addition, we use the model to estimate the maximum attainable actuation performance of Peano-HASEL actuators that are based on commercially-available, high-performance dielectric films.

* Corresponding author at: Department of Mechanical Engineering, University of Colorado, Boulder, CO 80309, USA.
E-mail address: Christoph.Keplinger@colorado.edu (C. Keplinger).

https://doi.org/10.1016/j.eml.2019.100449
2352-4316/

2. Analytical model for Peano-HASEL actuators

A linearly-contracting Peano-HASEL actuator (Fig. 1A) is comprised of rectangular pouches — which are formed by bonding flexible but inextensible polymer films into shells, filling the shell with a liquid dielectric, and placing a pair of electrodes on either side of the resulting pouch (Fig. 1B). As a voltage (typically on the order of kilovolts) is applied to these actuators, the Maxwell stress [24] displaces the liquid dielectric, causing the electrodes to zip together from the edge of the pouch, where the electrodes are closest together, and the electric field is the highest (Fig. 1C, Movie S1). As the electrodes zip together, the inextensibility of the shell and the incompressibility of the liquid dielectric causes the lower portion of the pouch to become more cylindrical, leading to an overall linear contraction (Δx) of the pouch (Fig. 1D). The progressive zipping of electrodes provides controllable actuation and reduces pull-in instabilities, as observed in previously-demonstrated electrostatic zipping actuators [25–28].

In this section, we derive an analytical model for the deformation of the actuator, when it is subjected to a static load and an electric field. We employ a global energy minimization approach, in which we consider the contribution from all components of the actuator to the free energy of the entire system. This approach allows us to calculate the deformation of the actuator without determining the electric field inside of the liquid dielectric and has been successfully used in previous works to model electrostatic zipping actuators [26,27,29,30]. To derive the model, we first parameterize the shape of the actuator to describe it with a single degree of freedom. The parameterization is similar to that used by Moretti et al. [29] who derived a numerical model for the deformation of Peano-HASEL actuators. We then define an equation for the free energy of the system. Finally, we minimize the free energy to derive an analytical expression for the equilibrium state of the actuator.

2.1. Parameterization of the geometry

A pouch (Fig. 2) is formed by bonding two rectangular dielectric films of length L_p, thickness t, and width w (out of the plane of the page) at the edges. In the range of parameters that we investigated experimentally, the dielectric film can be treated as an inextensible membrane without bending stiffness (Fig. S1; the effects of bending stiffness are introduced in Section 4.2). With this assumption, the surfaces of the liquid-filled pouch take a cylindrical shape such that the cross-section consists of two intersecting circular segments (Fig. 2A) [29,31,32]. The circular segments have a radius r_0, a central angle $2\alpha_0$, and an arc length equal to the undeformed length of the pouch, L_p. The volume of fluid in the pouch determines the cross-sectional area A. The initial-state value α_0 can then be described by

$$A = \frac{1}{2}L_p^2\left(\frac{\alpha_0 - \sin(\alpha_0)\cos(\alpha_0)}{\alpha_0^2}\right), \tag{1}$$

and the initial length of the actuator becomes

$$h = L_p\left(\frac{\sin(\alpha_0)}{\alpha_0}\right). \tag{2}$$

At the top, on both sides of the actuator, electrodes of length L_e and width w are attached to the dielectric film (Fig. 2A). When a voltage is applied to the electrodes, the dielectric films zip together over a length l_e, starting from the edge of the pouch (Fig. 2B). Ignoring any contribution to thickness from the liquid dielectric between the zipped electrodes, the final separation of the electrodes is twice the thickness of the film ($2t$). Because the membrane is inextensible, and the liquid is incompressible (L_p, w, and A remain constant during deformation), the actuator becomes shorter. During contraction, the fluid-filled region of the pouch retains the shape of cylindrical segments. We describe the geometry of this region with the central angle 2α. The arc length, l_p can be expressed by

$$l_p(\alpha) = \sqrt{\frac{2A\alpha^2}{\alpha - \sin(\alpha)\cos(\alpha)}}, \tag{3}$$

and the zipped length of the electrodes by

$$l_e(\alpha) = L_p - l_p(\alpha). \tag{4}$$

The stroke of the actuator becomes

$$x(\alpha) = h - \left(l_p(\alpha)\frac{\sin(\alpha)}{\alpha} + l_e(\alpha)\right). \tag{5}$$

The maximum stroke (Fig. 2C) is determined by two scenarios: (1) when the electrodes are completely zipped ($l_e = L_e$) or (2) when the fluid-filled region takes a circular cross-section ($\alpha = \pi/2$). At $\alpha = \pi/2$ further deformation is geometrically blocked because it requires a reduction in cross sectional area, which is prevented by the incompressibility of the liquid. To define the maximum zipping length, l_{max} for the second scenario, we substitute $\alpha = \pi/2$ into Eq. (4) and find that $l_{max} = L_p - \sqrt{\pi A}$ for a given L_p and A. Then the angle α_f that occurs at the maximum stroke is determined by:

$$1)\ L_e \le l_{max} \rightarrow \text{ solve } L_e = L_p - l_p(\alpha_f) \text{ for } \alpha_f \quad \text{(electrodes fully zipped).} \tag{6}$$

$$2)\ L_e \ge l_{max} \rightarrow \alpha_f = \frac{\pi}{2} \quad \text{(geometric blocking, electrodes not fully zipped).} \tag{7}$$

At the threshold between these two scenarios ($L_e = l_{max}$), geometric blocking occurs as the electrodes fully zip, and $\alpha_f = \pi/2$.

2.2. Total free energy of the system

The total free energy of the system includes the mechanical and electrical energy stored in the actuator, the contribution from an external force F interacting with the actuator, as well as the electrical energy exchanged with a battery of constant voltage V (Fig. 2D). Because we assume that the dielectric film is inextensible, and its bending stiffness can be neglected, the mechanical energy stored in the actuator is negligible, and only the energy stored in the electric field contributes to the free energy of the actuator. We further assume that the only contribution to the electrical energy comes from the region where the electrodes are zipped together, as the electric field in the unzipped region rapidly decays [29]. The capacitance of the zipped region can be described by

$$C(\alpha) = \frac{\varepsilon_r\varepsilon_0 w}{2t}l_e(\alpha), \tag{8}$$

where ε_r is the relative permittivity of the dielectric film, and ε_0 is the permittivity of free space. When charges Q are deposited on the capacitor, the electrical free energy U_e stored is (Fig. 2D)

$$U_e = \frac{1}{2}\frac{Q^2}{C(\alpha)}. \tag{9}$$

The electrical energy source can be represented by a battery of constant voltage V (Fig. 2D). When charges Q flow from this battery to the actuator, the free energy of the battery decreases

by -QV. We assume that a constant force F acts on the actuator (Fig. 2D) and that the actuator does work $Fx(\alpha)$ during contraction.

The total free energy of the system U_t can be described by the sum of the contributions from the actuator, the battery, and the force by

$$U_t(\alpha, Q) = \frac{1}{2}\frac{Q^2}{C(\alpha)} - QV + Fx(\alpha). \tag{10}$$

Using the fact that Q and V are linked by the capacitance (Q=CV), Eq. (10) can be simplified to

$$U_t(\alpha) = Fx(\alpha) - \frac{1}{2}C(\alpha)V^2. \tag{11}$$

2.3. Equation of state of the system

When the system reaches equilibrium, the free energy of the system minimizes with respect to α. Fig. 2E visualizes the change in free energy for this system as α changes from α_0 to α_f. For a given force F, up to a critical voltage, Eq. (11) does not have a minimum for $\alpha > \alpha_0$. Below this voltage, the actuator therefore does not deform (Fig. 2E, $V = V_1$). Above that critical voltage, there is a minimum at $\alpha > \alpha_0$. Minimizing Eq. (11) and solving for the applied force F leads to the equation

$$F = \frac{w}{4t}\frac{\cos(\alpha)}{1-\cos(\alpha)}\varepsilon_0\varepsilon_r V^2 \tag{12}$$

or

$$F = wt\frac{\cos(\alpha)}{1-\cos(\alpha)}\varepsilon_0\varepsilon_r E^2 \tag{13}$$

if expressed in terms of electric field, $E = V/2t$. The actuation strain of the actuator $\epsilon = x/h$ can be expressed from Eqs. (2) and (5) by

$$\epsilon = 1 - \frac{\alpha_0}{\sin(\alpha_0)}\left(1 + \frac{\sqrt{2A}}{L_p}\frac{\sin(\alpha)-\alpha}{\sqrt{\alpha - \sin(\alpha)\cos(\alpha)}}\right). \tag{14}$$

Eqs. (12)–(14) are solved for $\alpha_0 \le \alpha \le \alpha_f$ to produce a force-strain curve parametrized by α.

2.4. Characteristic force-strain curves

Using Eqs. (13) and (14), the predicted force-strain behavior and actuator scaling behavior can be examined. To simplify further analysis, we constrain the parameter space so that fully-zipped electrodes coincide with a circular pouch shape ($\alpha_f = \pi/2$, the threshold between Eqs. (6) and (7)). This optimum fill amount allows the maximum strain that is geometrically possible, while avoiding stray capacitance from additional electrode material covering part of the liquid-filled section of the fully-zipped pouch. With this requirement, the relationship between electrode length, pouch length, and cross-section satisfies

$$A = \frac{(L_p - L_e)^2}{\pi}. \tag{15}$$

Combining Eqs. (1) and (15), we can relate the fraction of the pouch length that is covered by electrodes $f_e \equiv L_e/L_p$ to the initial angle α_0 for the case of optimum filling:

$$f_e = \frac{L_e}{L_p} = 1 - \sqrt{\frac{\pi}{2}\left(\frac{\alpha_0 - \sin(\alpha_0)\cos(\alpha_0)}{\alpha_0^2}\right)}. \tag{16}$$

$f_e = 0$ corresponds to no electrodes (a completely filled pouch with $\alpha_0 = \pi/2$), and $f_e = 1$ corresponds to a pouch fully covered by electrodes (an unfilled flat pouch with $\alpha_0 = 0$).

Fig. 3A plots normalized (i.e. dimensionless) force-strain curves for Peano-HASEL actuators with different electrode coverage f_e. The calculated curves reproduce the force-strain behavior observed previously in Peano-HASEL actuators [14]. Varying the electrode coverage changes the overall shape of the curves, as well as their y- and x-intercepts. The y-intercept corresponds to the blocking force F_b, which denotes the maximum force generated by the actuator with no displacement. The x-intercept corresponds to free strain ϵ_f of the actuator, the actuation strain when no load is applied to the actuator. The blocking force increases monotonically with increasing electrode coverage (Fig. 3B), whereas the free strain increases to a maximum of 23% at $f_e = 0.19$, then decreases gradually with increased coverage (Fig. 3B).

2.5. Scaling predictions for the model

To predict the scaling behavior of Peano-HASEL actuators, we examine Eqs. (13) and (14). Under the condition of Eq. (15), the initial angle α_0 only depends on f_e (Eq. (16)). The relationship between ϵ and α is therefore independent of any other geometric or material parameters. The scaling behavior of Peano-HASEL actuators can therefore be determined solely from Eq. (13), which predicts the following behavior:

(1) F is independent of pouch length L_p
(2) F scales linearly with pouch width w
(3) F scales linearly with film thickness t, for a given electric field E.
(4) F depends on a Maxwell stress term, $\varepsilon_0\varepsilon_r E^2$ [24], where ε_r is the permittivity of the film, and $E = V/2t$ is the electric field in the zipped region of the electrodes.

In the following section, we experimentally confirm this scaling behavior.

3. Experimental validation of the model

In this section, we provide experimental validation of the analytical model for different geometries, materials, and voltages. We discuss the agreement between model and experiment.

3.1. Experimental characterization of Peano-HASEL actuators

Single-pouch Peano-HASEL actuators were constructed and tested as described in detail in *Supplementary Materials*. Pouches of various geometries were sealed using a CNC heat-sealer, as previously demonstrated by Mitchell et al. [33]. All actuators were constructed such that electrodes covered 50% of the pouch length ($f_e = 0.5$) and filled with the proper amount of liquid (Table S1) to ensure that fully-zipped electrodes resulted in a nearly circular cross-section in fluid-filled region of the pouch. All tests used LiCl-swelled PAAm hydrogel electrodes [34,35] (Fig. S2), Cargill Envirotemp FR3 liquid dielectric, and one of three heat-sealable shell materials: (1) 18-μm BOPP film, purchased from Multi-Plastics, Inc (type 5020), with $\varepsilon_r = 2.2$ [36], (2) 11-μm BOPP film, provided by Bolloré Plastic Films Division, with $\varepsilon_r = 2.2$, and (3) 35-μm TPU Polyester film provided by American Polyfilm, Inc. (type VLM-3301) with $\varepsilon_r = 6.9$. The film thicknesses were confirmed using micrometers, while TPU permittivity was determined using impedance measurements (see *Supplemental Materials*). An exemplary 18-μm BOPP actuator with $L_p = 2$ cm and $w = 12$ cm is shown in Fig. 4A with a schematic showing actuator shape and dimensions in Fig. S3. A large ratio of width w to length L_p was used whenever possible to reduce the impact of end constraints on actuation [37]. The actuation signal was a 0.5 Hz square wave voltage that used reversing polarity (Fig.

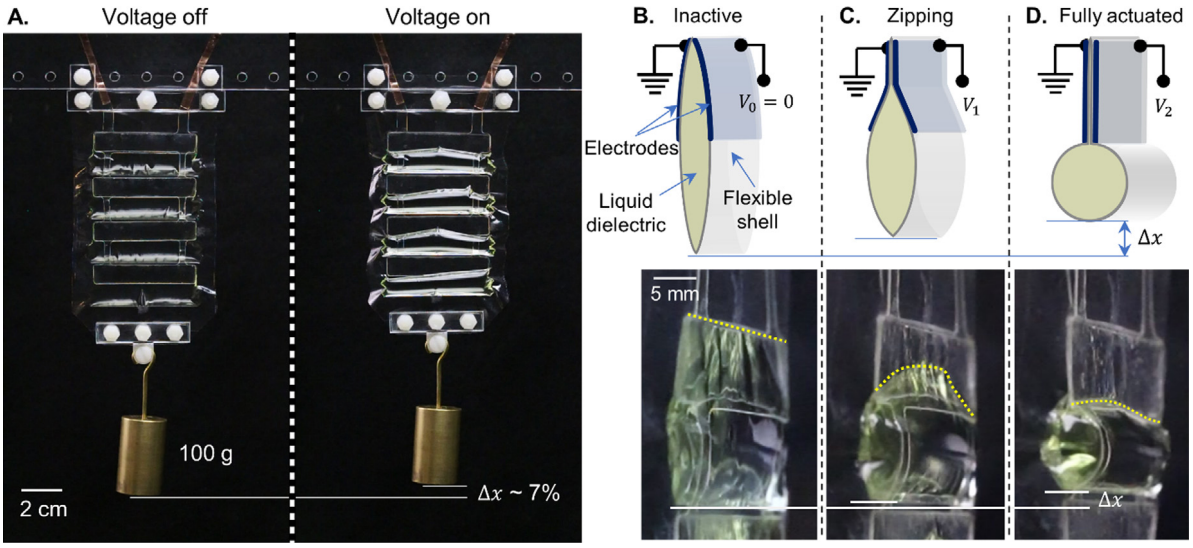

Fig. 1. Zipping mechanism in Peano-HASEL actuators. (A) A four pouch Peano-HASEL lifting a 100g load at an applied voltage of 9 kV, reaching an actuation stroke Δx that corresponds to 7% actuation strain. (B) A schematic of a single pouch in the inactive state shows the basic components of the actuator. The photograph below the schematic shows a single pouch from the actuator in (A) for comparison. (C) On application of a voltage V_1, the Maxwell stress causes the electrodes to zip together starting at the top of the pouch — the region of smallest electrode separation and thus highest electric field. This displaces the liquid dielectric into the bottom of the pouch, leading to contraction of the structure. (D) As the voltage increases, the zipping progresses until the actuator reaches a fully contracted state, with the electrodes completely zipped together.

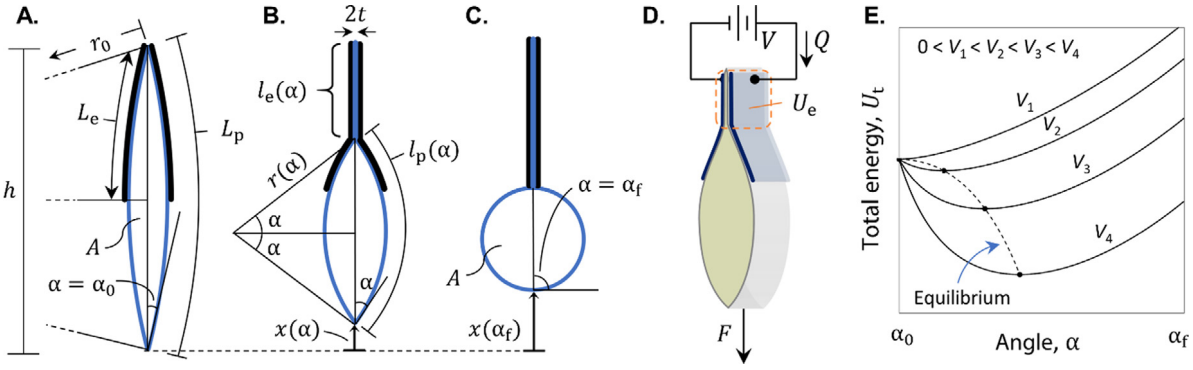

Fig. 2. Analytical model for Peano-HASEL actuators. (A) Parameterization of the Peano-HASEL pouch shape in the inactive state, (B) partially actuated state, and (C) fully actuated state. A is the cross-sectional area of the pouch, which remains constant during contraction. The width of the pouch w (not shown) is into the page. (D) Model of the Peano-HASEL actuator for determining the free-energy of the actuator system, where QV is the energy exchanged with a battery, U_e is the electrical energy stored in the zipped region of the actuator, and $Fx(\alpha)$ is the work done on a constant external load. For large ratios of $L_p : t$, the bending stiffness of the inextensible shell can be neglected (Fig. 7C). (E) Total energy U_t of a Peano-HASEL system as a function of zipping angle at several voltages. The minimum of each curve corresponds to the equilibrium state of the system. As the voltage increases, the equilibrium shifts to larger angles, leading to a larger displacement x.

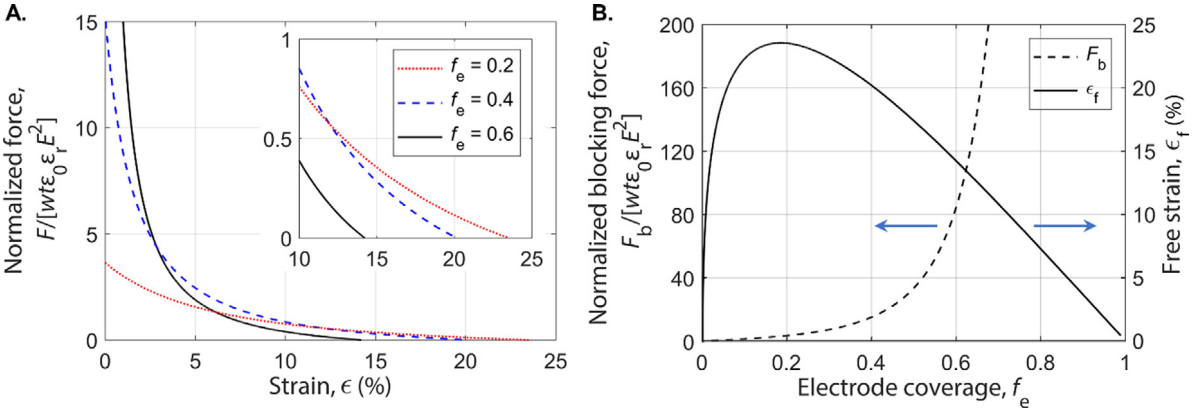

Fig. 3. Characteristics of force-strain relationships of Peano-HASEL actuators. (A) Force-strain behavior of Peano-HASEL actuators for different electrode coverage $f_e \equiv L_e/L_p$ when the cross-section A is chosen such that $\alpha_f = \pi/2$. The inset shows a zoomed view of the plot in the high strain region. (B) Normalized blocking force F_b and free strain ϵ_f of the actuator as a function of electrode coverage. The blocking force increases monotonically with increasing f_e, while the free strain reaches a maximum at $f_e = 0.19$ then decreases with increasing f_e.

S4) to mitigate any space charge development in the actuator over successive cycles. Displacement was measured with video tracking for various fixed loads, which were provided by brass weights. Movie S2 shows two of these BOPP actuators contracting under load.

3.2. Experimental results and comparison to model

To demonstrate the general validity of our analytical model, we compare theoretical prediction to experimental force-strain data for actuators with differing conditions (t, w, L_p, ε_r, E, V), as presented in Fig. 4B, and find good agreement across all tested actuators without relying on any fitting parameters. From here, the specific scaling behaviors outlined in Section 2.4 were confirmed by selectively varying actuator parameters to isolate their effect on force-strain behavior, as discussed below.

To investigate width-scaling behavior, force-strain curves were measured for actuators with pouch lengths L_p of 2 cm and widths w varying between 3 cm and 15 cm (Fig. S5A). When normalizing the force data by w, all data collapsed onto a single curve (Fig. 4C), confirming the linear width-scaling behavior predicted by the model. The narrowest pouch width showed slightly degraded performance, likely due to increased end constraints [37]. The model agrees well with the data, consistently slightly over-predicting the load, which suggests an additional effect other than end constraints that reduces the actuator performance. We attribute this effect to a residual layer of liquid dielectric between the zipped films, which increases electrode separation and reduces the electric field between the zipped electrodes.

To investigate scaling behavior with pouch length, force-strain curves were measured for actuators with widths of 12 cm and pouch lengths varying between 1.5 cm and 4 cm (Fig. 4D). As predicted theoretically, there is no observable dependence of the actuation force on the pouch length.

To investigate the thickness-scaling behavior, force-strain curves were measured for actuators with widths of 9 cm, pouch lengths of 2 cm, and film thicknesses of 11 μm and 18 μm (Fig. S5B). A constant electric field of $\sim$ 225 V/μm was maintained in the zipped region by using voltages of 4.8 kV (11-μm film) and 8 kV (18-μm film). The force data was normalized by film thickness t in order to collapse experimental data to a single curve, confirming that force output of Peano-HASEL actuators increases linearly with the film thickness, while maintaining a constant electric field E.

Finally, we investigated the dependence of the force-strain behavior of the actuator on the Maxwell stress, $\varepsilon_0\varepsilon_r E^2$, present in the zipped region of the films. Actuators were constructed with widths of 6 cm and pouch lengths of 2 cm using 35-μm TPU polyester film ($\varepsilon_r = 6.9$) and 18-μm BOPP film ($\varepsilon_r = 2.2$). The force-strain behavior of these actuators was measured and compared to model predictions (Fig. S5C). When normalized by Maxwell stress all measured data collapsed onto one curve (Fig. 4F), confirming that actuation force scales with Maxwell stress, as with DEAs [24]. We find good agreement between model and experiment for all data, with slightly better agreement for TPU polyester than BOPP.

3.3. Actuator behavior under high loads

Increasing the load on the actuator reduces the actuation strain until the blocking force F_b is reached, above which any displacement of the actuator is prevented (Fig. 3). To validate the predicted blocking forces, we compared the model predictions and experimental results for two actuators with widths of 12 cm and 9 cm at high loads. These were actuated with voltages of 4 kV and 8 kV respectively.

We observed good agreement across the investigated range of loads up to the blocking force, as shown in Fig. 5A. The predicted blocking forces were within 15% of measured values. Fig. 5B shows the 9 cm wide actuator under a 4.5 kg load, which corresponded to its blocking force at 8 kV. At high loads, actuators performed better than predicted by the model; at these loads, an instability caused asymmetric zipping of the electrodes, which led to a simultaneous contraction and rotation of the free end of the actuator. This instability allows for larger zipping areas for the same actuation strain, which leads to more electrical energy stored in the zipped region of the actuator and consequently increases output force. Movie S3 shows these instabilities for high loads and demonstrates their reduction at higher frequencies of actuation.

4. Roadmap for improved performance

Having experimentally validated the analytical model across a range of conditions, we now look towards performance characteristics and trends that will be useful to inform future designs and improvements of HASEL actuators. First, we explore how electrode coverage can be used as a method for tuning the force-strain response of Peano-HASELs to optimize for maximum load, strain, or a combination of the two. Next, we discuss avenues for drastically increasing the specific energy of actuators.

4.1. Effects of electrode coverage on force-strain behavior

While all fabricated Peano-HASEL actuators used an electrode coverage $f_e = 0.5$, this may be adjusted to alter the shape of the desired force-strain curve, as seen in Fig. 3A for three specific values of f_e. Here we analyze this trend in more detail to see how actuation strain varies as a function of electrode coverage and force. Fig. 6A shows the contractile strain of modeled BOPP Peano-HASEL actuators with $w = 5$ cm, $L_p = 2$ cm, $t = 18$ μm, and $E = 225$ V/μm, as a function of output force F and electrode coverage. As electrode coverage changes, so does the liquid fill amount, to ensure a circular cross-section when the electrodes are fully zipped together (Eq. (15)). From the plot we see a trade-off between strain and force for varying f_e. Lower values of f_e lead to larger maximum strains at lower forces, while larger f_e lead to higher forces at low strains. A black dashed line shows the electrode coverage that results in the highest force output for a given strain. We see this line shifts to higher electrode coverage for higher loads. Fig. 6B models the same actuators operating at $E = 700$ V/μm, a typical breakdown strength for BOPP [38]. This plot shows the same general behavior, with increased force output. Taken together, these plots demonstrate a range of tunability that allows for designing actuators with specific force-strain characteristics depending on expected loads and desired strains.

4.2. Increasing the specific energy of Peano-HASEL actuators

When comparing the performance of different types of actuators, the specific energy – a measure of the output work of an actuator normalized to the actuator mass – is an important metric for comparison. The most general method for calculating specific energy, and the method used in this section, involves integrating under the actuator's force–displacement curve to get output work, then normalizing to the mass of the actuator.

As shown previously in Fig. 4D, changing the pouch length L_p has no impact on force-strain characteristics; however, reducing L_p has two effects: it decreases the actuator cross-section – and consequently the mass of the actuator – quadratically (Eq. (1)),

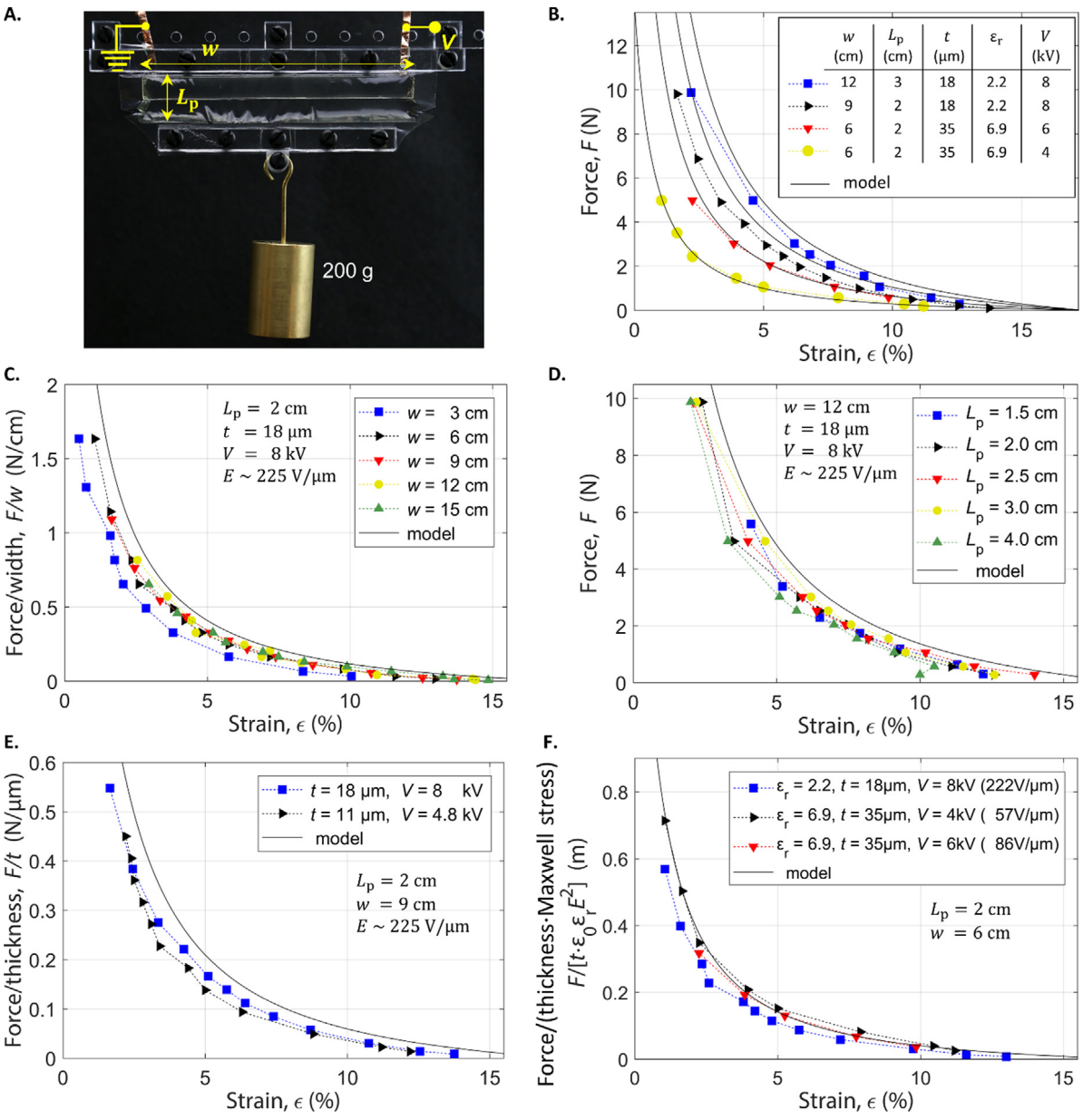

Fig. 4. Experimental validation of modeling results. (A) Photograph of a single-pouch actuator used for the experimental tests, with a 200 g mass attached. (B) Comparison of experimental force-strain curves with model prediction across a range of different geometries, materials, and testing parameters. (C) Calculated and experimental force-strain curves for Peano-HASEL actuators normalized by the width w of the pouch. The agreement between model and experimental data improves as the pouches become wider. (D) The calculated and experimental force-strain curves show no dependence on the length of the pouch L_p. (E) Calculated and experimental force-strain curves normalized by the film thickness t, actuated at different voltages to maintain the electric field at $E \sim 225$ V/μm. (F) Calculated and experimental force-strain curves normalized by thickness and the Maxwell stress, $\varepsilon_0\varepsilon_r E^2$, highlighting the fact that the Maxwell stress governs actuation in Peano-HASELs.

and it linearly decreases the actuator stroke. By connecting multiple short actuators in series, the force-stroke characteristic of a single large actuator can therefore be achieved at reduced actuator mass, and consequently increased specific energy (Fig. 7A). Shorter pouch length also leads to increased actuation stress (Fig. 7B), when multiple actuators are put in parallel, as it decreases the radius R of the liquid-filled region of the actuators in the fully-contracted state, and allows for a closer actuator spacing that scales linearly with L_p, when ignoring the contribution of the film thickness to the overall pouch radius R.

Based on the theoretical model, continually decreasing the pouch length increases the performance of Peano-HASEL actuators, both individually and in stacks. The model predicts that this trend continues to arbitrarily small dimensions (Fig. 7C). In reality, as the pouch length decreases, the bending stiffness of the film becomes non-negligible, and will act to reduce the actuation strain. Here, to approximate the influence of the bending stiffness of the film on the actuation behavior, we add an additional term to the total energy of the system that accounts for the energy required to bend the film into a cylindrical shape (see *Supplemental Materials*). This term begins to noticeably influence actuation performance below a certain threshold of $L_p{:}\,t$ until it completely suppresses actuation (Fig. 7C). While the simplified model we use here does not give quantitatively accurate results for very small values of $L_p{:}\,t$ (region of the solid curve in Fig. 7C to the left of the peak value for specific energy), it does allow us to obtain a good estimate for specific energy up to the peak value when decreasing the pouch length (region of the solid curve in Fig. 7C to the right of the peak value). Determining the exact actuation behavior in the range of very small values of $L_p{:}\,t$ would require detailed

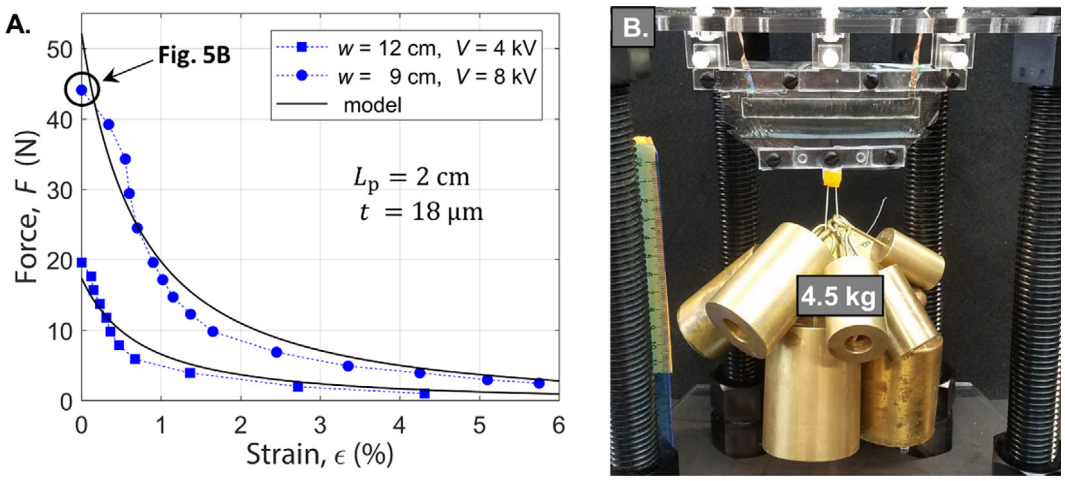

Fig. 5. Model predictions under high-load, low-strain conditions. (A) Calculated and experimental force-strain curves at high loads for actuators made from BOPP film. The theoretical prediction closely matches the experimental data up to the blocking force — the intercept of the curves with the y-axis. (B) 9-cm wide actuator with a 4.5-kg load that corresponded to its blocking force (data point circled in (A)).

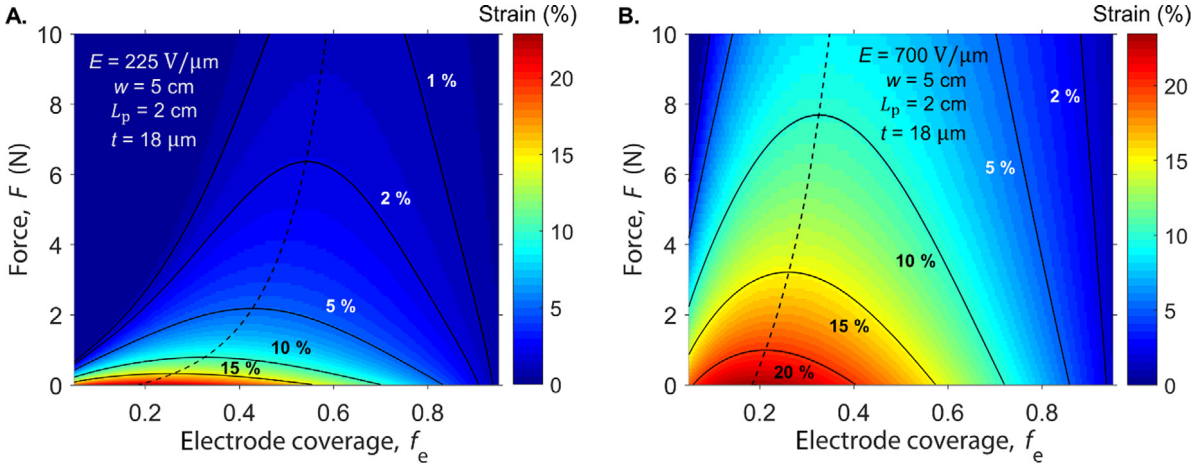

Fig. 6. Tuning the force-strain characteristics of Peano-HASEL actuators by varying electrode coverage. The colored contours indicate the calculated actuation strain of Peano-HASEL actuators as a function of electrode coverage and applied force. A vertical slice of the contour plot (for a given electrode coverage f_e) reproduces a force-strain curve for a specific Peano-HASEL actuator. (A) Actuation strain at $E = 225$ V/μm. The dashed line corresponds to the electrode coverage that results in the highest achievable strain for a given load. (B) Actuation strain at $E = 700$ V/μm — a typical value reported for the dielectric strength of BOPP [38].

modeling of the bending behavior of the pouch, including the influence of the end constraints, using plate theory [39], which is beyond the scope of this paper.

In Figs. 7D–F we examine the interplay of pouch length and film thickness in determining the specific energy E_s of Peano-HASEL actuators. Fig. 7D shows the specific energy for actuators made from BOPP under application of an electric field of 225 V/μm — the same conditions used in experimental testing for Figs. 4C–E. These results include the contribution of the mass of the shell material to total actuator mass, which becomes important for small ratios of L_p:t. We assume a density of ρ = 0.96 g/cm^3 for the liquid dielectric (FR3) [40] and a density of ρ = 0.9 g/cm^3 for the shell (BOPP) [36]. A Young's modulus of 2.5 GPa and a Poisson's ratio of 0.33 are assumed for the BOPP [36,41]. The mass of the electrodes is neglected, as they may be produced in ultrathin (< 1 μm) layers using a variety of methods such as inkjet printing [42]. As seen in Fig. 7D, the specific energy increases as the pouch length is reduced, before quickly falling to zero as the bending stiffness begins to dominate and reduce actuation. An ellipse encloses the range of theoretical specific energies for the actuators used in Fig. 4D (2.9 J/kg at L_p= 40 mm to 7.7 J/kg at L_p = 15 mm). Specific energies up to 35 J/kg are possible by simply reducing L_p to 1 mm for BOPP with t = 18 μm at E = 225 V/μm — a value that is on par with typical natural muscle [12]. Furthermore, reduced operating voltages can be achieved without changing the specific energy by reducing both pouch length and film thickness in tandem, such that L_p:t remains constant (moving along the contour lines in Fig. 7D). Increasing the applied electric field to the breakdown strength of BOPP (700 V/μm [38]) (Fig. 7E), actuators with current dimensions (L_p = 2 cm, t = 18 μm) are predicted to achieve specific energies of 50 J/kg. By decreasing pouch length to roughly 0.5 mm, the model predicts specific energies up to 720 J/kg (Fig. 7E).

The model suggests that optimizing the electrical properties of the dielectric film can have a drastic impact on the performance of actuators. Fig. 7F shows the predicted performance of an actuator made from a commercially-available PVDF terpolymer [43], with a breakdown strength of 600 V/μm and ε_r = 50, assuming ρ = 1.7 g/cm^3 and a Young's Modulus of 200 MPa [44]. The model predicts specific energies up to 19,000 J/kg, which exceeds the performance of all current artificial muscle technologies [12]. These predictions emphasize the high electrical forces that can be generated in Peano-HASEL actuators. In practice, creating actuators with high specific energies will require more detailed

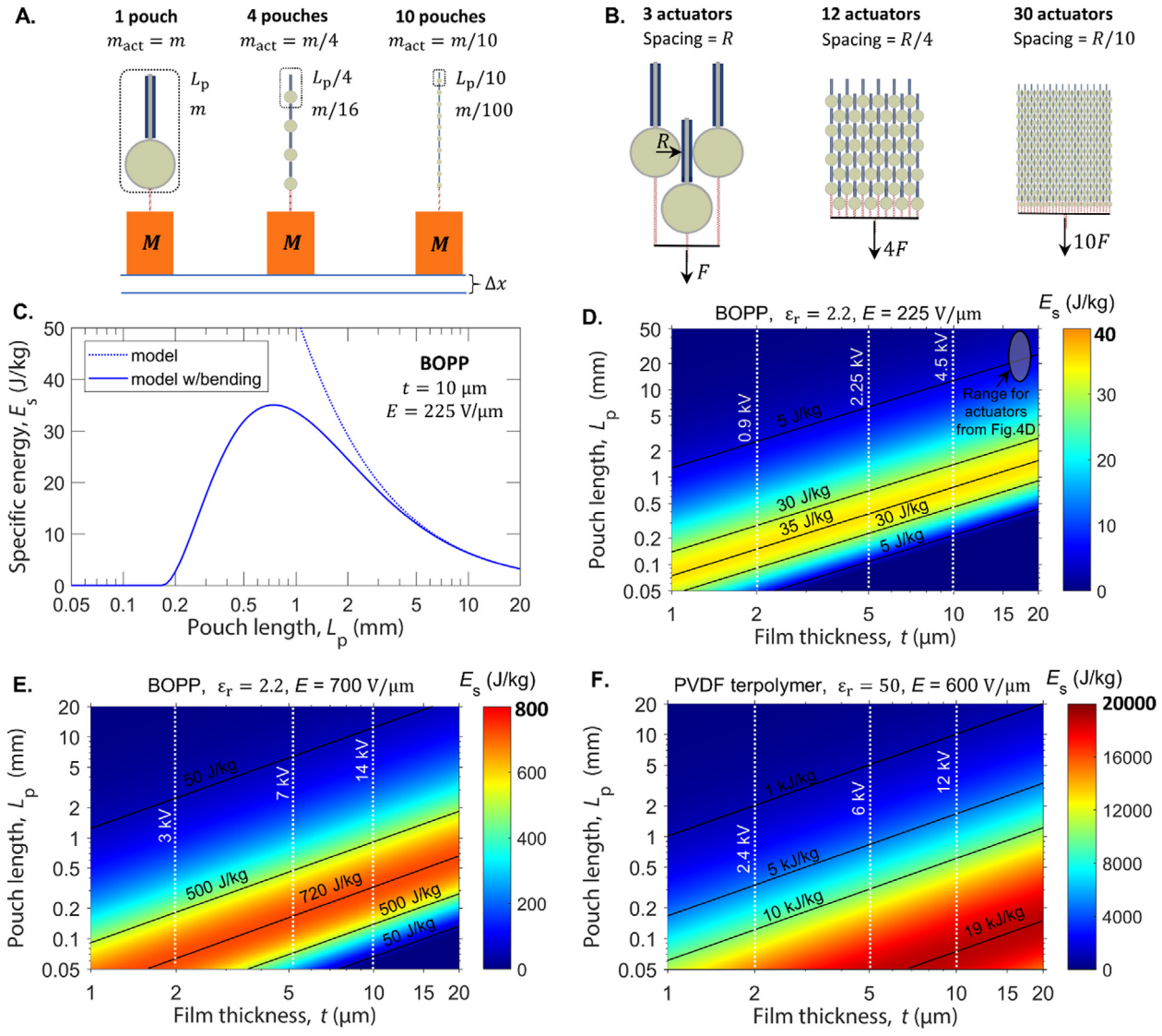

Fig. 7. Increasing the actuation stress and specific energy of Peano-HASEL actuators. (A) Starting with a single pouch of length L_p and mass m, the specific energy E_s of an actuator can be increased by decreasing pouch length, which does not influence the force-strain characteristics, but reduces the mass of a single pouch, and consequently the mass of the actuator m_{act} (which is the mass of all pouches in series). (B) Actuators from (A) placed in parallel stacks with a stacking density that scales inversely with pouch length, when ignoring the thickness of the shell material. Increasing stacking density increases force output F of the stack linearly while holding the cross-section constant, which increases actuation stress. The mass of all stacks remains constant. (C) Specific energy as a function of pouch length for modeled BOPP actuators with $t = 10$ μm, $V = 4.5$ kV, E = 225 V/μm. Below a certain value of L_p the model that includes bending stiffness trends towards zero as the stiffness of the shell begins to dominate. (D) Colored contours indicate the calculated specific energy for Peano-HASEL actuators at different pouch lengths and film thicknesses, with $E = 225$ V/μm. Each vertical cross-section of the plot reproduces a curve similar to (C) with consideration of the bending stiffness. The ellipse at the top-right of the plot indicates the theoretical range of specific energies for the actuators tested in Fig. 4D. (E) Increasing the electric field to 700 V/μm (the reported breakdown strength of BOPP [38]) shifts the peak specific energy to smaller pouch lengths and results in calculated specific energies up to 720 J/kg. (F) For existing materials with high permittivity ($\varepsilon_r = 50$) and high breakdown strength ($E = 600$ V/μm) [43] the model predicts specific energies up to 19,000 J/kg.

consideration of the mechanical properties of the actuator. For instance, these results do not account for the mechanical strength of the polymer films, which will determine the maximum possible stress in the material. Furthermore, as pouch length decreases we expect that the effect of side constraints – which are neglected here – will become more prominent; new designs and geometries may be required to mitigate the effect of these constraints.

5. Conclusion

In this work, we derived an electromechanical model for linearly contracting Peano-HASEL actuators, and experimentally confirmed its validity across a range of actuator geometries, actuator materials, and operating conditions. This analytical model describes the data very well without the use of fitting parameters and enables us to predict the scaling behavior of Peano-HASEL actuators. A central result of this work shows that decreasing pouch length provides a way to drastically increase the specific energy of Peano-HASEL actuators. Model predictions estimate that specific energies > 10,000 J/kg are achievable by constructing Peano-HASELs using an existing electroactive polymer film (PVDF terpolymer) with high-performance electrical properties [43,44], and sub-mm pouch lengths. Similar feature sizes have been demonstrated for soft pneumatic actuators using lithographic techniques [45] — a method that could likely be applied to Peano-HASEL fabrication.

We note here that the analytical model presented in this work predicts the static performance of Peano-HASEL actuators and as such does not account for any dynamic effects such as the viscosity of the liquid dielectric and inertia; Kellaris et al. have shown

previously that these effects influence the dynamic response of actuators above a certain frequency [14]. Moreover, this model neglects the electric field in the liquid dielectric, and is therefore independent of the properties of the liquid dielectric. Given the agreement between model and experiment, we conclude that this assumption is valid for the materials and geometries tested. Under some operating conditions, the properties of the liquid dielectric must be considered, such as when the liquid dielectric has a much higher permittivity than the shell material; in these cases, the model must be modified. In addition, at fields higher than the dielectric strength of the liquid, electrical failure may occur in the liquid dielectric; interestingly, the electric field in the liquid in the experiments shown in this paper far exceeded the stated breakdown strength of the Cargill FR3 liquid dielectric (27 V/μm [40]). To fully understand potential performance and limitations of Peano-HASEL actuators, more research must be done on the fundamental characteristics of dielectric breakdown in composite solid–liquid dielectric structures.

This work provides the first theory-driven design approach for Peano-HASEL actuators and provides guidelines for the creation of Peano-HASELs with specific energies that could outperform current artificial muscle technologies [12]. Combined with the fast muscle-like actuation achievable in these devices [14], these strategies provide a roadmap for creating powerful and compact Peano-HASEL actuators that could be parallelized for high-strength applications, or used individually as lightweight actuators for high power density applications such as ornithopter flight [46,47]. Such improvements will enable the next-generation of artificial muscles for highly agile and capable soft robots.

Acknowledgments

This work was supported by start-up funds from the University of Colorado Boulder, USA, an National Science Foundation grant, USA grant for Cyber–Physical Systems (grant No. 1739452), and a Packard Fellowship from The David and Lucile Packard Foundation, USA. We also acknowledge funding from the Army Research Office (DURIP grant No. W911NF-18-1-0203), which was used to purchase laboratory equipment to characterize and fabricate actuators.

Conflict of interest

N.K. and C.K. are listed as inventors on PCT application (PCT/US19/02056 8) and PCT application (PCT/US18/023797) which cover fundamentals and basic designs of HASEL actuators. N.K., P.R., and C.K. are listed as inventors on a U.S. provisional patent application (62/813,266) which covers composite and folding designs of HASEL actuators. N.K. and C.K. are co-founders of Artimus Robotics, a start-up company commercializing HASEL actuators.

Appendix A. Supplementary data

Supplementary material related to this article can be found online at https://doi.org/10.1016/j.eml.2019.100449.

References

[1] S. Haddadin, E. Croft, Physical human–robot interaction, in: B. Siciliano, O. Khatib (Eds.), Handbook of Robotics, second ed., Springer, 2016, pp. 1835–1874, http://dx.doi.org/10.1007/978-3-319-32552-1.

[2] B. Matthias, S. Kock, H. Jerregard, M. Källman, I. Lundberg, R. Mellander, Safety of collaborative industrial robots: Certification possibilities for a collaborative assembly robot concept, in: 2011 IEEE Int. Symp. Assem. Manuf. ISAM 2011, IEEE, Tampere, 2011, http://dx.doi.org/10.1109/ISAM.2011.5942307.

[3] H. Yuk, S. Lin, C. Ma, M. Takaffoli, N.X. Fang, X. Zhao, Hydraulic hydrogel actuators and robots optically and sonically camouflaged in water, Nature Commun. 8 (2017) 14230, http://dx.doi.org/10.1038/ncomms14230.

[4] K. Kumar, J. Liu, C. Christianson, M. Ali, M.T. Tolley, J. Aizenberg, D.E. Ingber, J.C. Weaver, K. Bertoldi, A biologically inspired, functionally graded end effector for soft robotics applications, Soft Robot. 4 (2017) 317–323, http://dx.doi.org/10.1089/soro.2017.0002.

[5] M.T. Tolley, R.F. Shepherd, B. Mosadegh, K.C. Galloway, M. Wehner, M. Karpelson, R.J. Wood, G.M. Whitesides, A resilient, untethered soft robot, Soft Robot. 1 (2014) 213–223, http://dx.doi.org/10.1089/soro.2014.0008.

[6] K. Suzumori, S. Iikura, H. Tanaka, Development of flexible microactuator and its applications to robotic mechanisms, in: IEEE, Int. Conf. on Robotics and Automation (ICRA), Sacramento, 1991, http://dx.doi.org/10.1109/ROBOT.1991.131850.

[7] P. Polygerinos, Z. Wang, K.C. Galloway, R.J. Wood, C.J. Walsh, Soft robotic glove for combined assistance and at-home rehabilitation, Robot. Auton. Syst. 73 (2015) 135–143, http://dx.doi.org/10.1016/j.robot.2014.08.014.

[8] A. Rafsanjani, Y. Zhang, B. Liu, S.M. Rubinstein, K. Bertoldi, Kirigami skins make a simple soft actuator crawl, Sci. Robot. 3 (2018) eaar7555, http://dx.doi.org/10.1126/scirobotics.aar7555.

[9] S. Kim, C. Laschi, B. Trimmer, Soft robotics: A bioinspired evolution in robotics, Trends Biotechnol. 31 (2013) 287–294, http://dx.doi.org/10.1016/j.tibtech.2013.03.002.

[10] J.W. Booth, D. Shah, J.C. Case, E.L. White, M.C. Yuen, O. Cyr-choiniere, R. Kramer-bottiglio, OmniSkins : Robotic skins that turn inanimate objects into multifunctional robots, 3 (2018) eaat1853 (2018), http://dx.doi.org/10.1126/scirobotics.aat1853.

[11] L. Hines, K. Petersen, G.Z. Lum, M. Sitti, Soft actuators for small-scale robotics, Adv. Mater. 29 (2017) 160348, http://dx.doi.org/10.1002/adma.201603483.

[12] S.M. Mirvakili, I.W. Hunter, Artificial muscles: Mechanisms, applications, and challenges, Adv. Mater. 30 (2018) 170440, http://dx.doi.org/10.1002/adma.201704407.

[13] E. Acome, S.K. Mitchell, T.G. Morrissey, M.B. Emmett, C. Benjamin, M. King, M. Radakovitz, C. Keplinger, Hydraulically amplified self-healing electrostatic actuators with muscle-like performance, Science 359 (2018) 61–65, http://dx.doi.org/10.1126/science.aao6139.

[14] N. Kellaris, V.G. Venkata, G.M. Smith, S.K. Mitchell, C. Keplinger, Peano-HASEL actuators: Muscle-mimetic, electrohydraulic transducers that linearly contract on activation, Sci. Robot. 3 (2018) eaar3276, http://dx.doi.org/10.1126/scirobotics.aar3276.

[15] R. Pelrine, R. Kornbluh, Q. Pei, J. Joseph, High-speed electrically actuated elastomers with strain greater than 100%, Science 287 (2000) 836–839, http://dx.doi.org/10.1126/science.287.5454.836.

[16] E.F.M. Henke, S. Schlatter, I.A. Anderson, Soft dielectric elastomer oscillators driving bioinspired robots, Soft Robot. 4 (2017) 353–367, http://dx.doi.org/10.1089/soro.2017.0022.

[17] M. Duduta, E. Hajiesmaili, H. Zhao, R.J. Wood, D.R. Clarke, Realizing the potential of dielectric elastomer artificial muscles, Proc. Natl. Acad. Sci. (2019) 201815053, http://dx.doi.org/10.1073/pnas.1815053116.

[18] Y.F. Goh, S. Akbari, T.V.K. Vo, S. Jin, A. Koh, Electrically-induced actuation of acrylic-based dielectric elastomers in excess of 500% strain, Soft Robot. 5 (2018) 675–684, http://dx.doi.org/10.1089/soro.2017.0078.

[19] I.A. Anderson, T.A. Gisby, T.G. McKay, B.M. O'Brien, E.P. Calius, Multi-functional dielectric elastomer artificial muscles for soft and smart machines, J. Appl. Phys. 112 (2012) 041101, http://dx.doi.org/10.1063/1.4740023.

[20] G. Gu, J. Zhu, L.-M. Zhu, X. Zhu, A survey on dielectric elastomer actuators for soft robots, Bioinspir. Biomim. 12 (2017) 011003, http://dx.doi.org/10.1088/1748-3190/12/1/011003.

[21] B. Mosadegh, P. Polygerinos, C. Keplinger, S. Wennstedt, R.F. Shepherd, U. Gupta, J. Shim, K. Bertoldi, C.J. Walsh, G.M. Whitesides, Pneumatic networks for soft robotics that actuate rapidly, Adv. Funct. Mater. 24 (2014) 2163–2170, http://dx.doi.org/10.1002/adfm.201303288.

[22] R.V. Martinez, J.L. Branch, C.R. Fish, L. Jin, R.F. Shepherd, R.M.D. Nunes, Z. Suo, G.M. Whitesides, Robotic tentacles with three-dimensional mobility based on flexible elastomers, Adv. Mater. 25 (2013) 205–212, http://dx.doi.org/10.1002/adma.201203002.

[23] P. Polygerinos, N. Correll, S.A. Morin, B. Mosadegh, C.D. Onal, K. Petersen, M. Cianchetti, M.T. Tolley, R.F. Shepherd, Soft robotics: Review of fluid-driven intrinsically soft devices; manufacturing, sensing, control, and applications in human–robot interaction, Adv. Eng. Mater. 19 (2017) 170001, http://dx.doi.org/10.1002/adem.201700016.

[24] Z. Suo, Theory of dielectric elastomers, Acta Mech. Solida Sin. 23 (2010) 549–578, http://dx.doi.org/10.1016/S0894-9166(11)60004-9.

[25] P. Gebbers, C. Grätzel, L. Maffli, C. Stamm, H. Shea, Zipping it up: DEAs independent of the elastomer's electric breakdown field, in: SPIE, Electroact. Polym. Actuators Devices, EAPAD, 2012, p. 83402P, http://dx.doi.org/10.1117/12.915020.

[26] L. Maffli, B. O'Brien, S. Rosset, H. Shea, Pump it up, in: SPIE, Electroact. Polym. Actuators Devices, EAPAD, 2012, p. 83402Q, http://dx.doi.org/10.1117/12.914831.
[27] L. Maffli, S. Rosset, H.R. Shea, Zipping dielectric elastomer actuators: Characterization, design and modeling, Smart Mater. Struct. 22 (2013) 104013, http://dx.doi.org/10.1088/0964-1726/22/10/104013.
[28] J. Li, Electrostatic Zipping Actuators and their Application to MEMS, Massachusetts Institute of Technology, 2004.
[29] G. Moretti, M. Duranti, M. Righi, R. Vertechy, M. Fontana, Analysis of dielectric fluid transducers, in: Y. Bar-Cohen (Ed.), SPIE, Electroact. Polym. Actuators Devices (EAPAD) XX, 2018, p. 105940W, http://dx.doi.org/10.1117/12.2297082.
[30] M.T.A. Saif, B.E. Alaca, H. Sehitoglu, Analytical modeling of electrostatic membrane actuator for micro pumps, J. Microelectromech. Syst. 8 (1999) 335–345.
[31] R. Niiyama, D. Rus, S. Kim, Pouch Motors: Printable/inflatable soft actuators for robotics, in: 2014 IEEE Int. Conf. Robot. Autom., ICRA, 2014, pp. 6332–6337, http://dx.doi.org/10.1109/ICRA.2014.6907793.
[32] S. Sanan, P.S. Lynn, S.T. Griffith, Pneumatic torsional actuators for inflatable robots, J. Mech. Robot. 6 (2014) 031003, http://dx.doi.org/10.1115/1.4026629.
[33] S.K. Mitchell, X. Wang, E. Acome, T. Martin, K. Ly, N. Kellaris, V.G. Venkata, C. Keplinger, An easy-to-implement toolkit to create versatile and high-performance HASEL actuators for untethered soft robots, under revision.
[34] Y. Bai, B. Chen, F. Xiang, J. Zhou, H. Wang, Z. Suo, Transparent hydrogel with enhanced water retention capacity by introducing highly hydratable salt, Appl. Phys. Lett. 105 (2014) 151903, http://dx.doi.org/10.1063/1.4898189.
[35] C. Keplinger, J.Y. Sun, C.C. Foo, P. Rothemund, G.M. Whitesides, Z. Suo, Stretchable, transparent, ionic conductors, Science 341 (2013) 984–987, http://dx.doi.org/10.1126/science.1240228.
[36] Comparative data for plastic films, datasheet, 2018, https://www.m-petfilm.de/en/service/comparative-data-for-plastic-films/. (Accessed 6 December 2018).
[37] A.J. Veale, S.Q. Xie, I.A. Anderson, Characterizing the Peano fluidic muscle and the effects of its geometry properties on its behavior, Smart Mater. Struct. 25 (2016) 065013, http://dx.doi.org/10.1088/0964-1726/25/6/065013.
[38] J. Ho, R. Jow, Characterization of High Temperature Polymer Thin Films for Power Conditioning Capacitors, 2009 Army Research Laboratory, 2009, https://www.arl.army.mil/arlreports/2009/ARL-TR-4880.pdf.
[39] S.P. Timoshenko, S. Woinowsky-Krieger, Theory of Plates and Shells, McGraw-hill, New York, 1959, https://scholar.google.com/scholar?hl=en&as_sdt=0%2C6&q=timoshenko+theory+of+plates+and+shells&btnG.
[40] Envirotemp FR3 fluid datasheet, 2016, https://www.cargill.com/doc/1432076501923/envirotemp-fr3-r2000-tds.pdf. (Accessed 6 December 2018).
[41] G.N. Greaves, A.L. Greer, R.S. Lakes, T. Rouxel, Poisson's ratio and modern materials, Nat. Mat. 10 (2011) 823–837, http://dx.doi.org/10.1038/nmat3134.
[42] C.A. de Saint-Aubin, S. Rosset, S. Schlatter, H. Shea, High-cycle electromechanical aging of dielectric elastomer actuators with carbon-based electrodes, Smart Mater. Struct. 27 (2018) 074002, http://dx.doi.org/10.1088/1361-665X/aa9f45.
[43] S. Zhang, C. Zou, X. Zhou, D. Anderson, B. Zellers, Q. Zhang, Polymer film capacitors with high dielectric constant, high capacitance density, and high energy density, in: IEEE, Int. Power Modul. High Volt. Conf., 2010, pp. 221–224 http://dx.doi.org/10.1109/IPMHVC.2010.5958333.
[44] Solvene T EAP technical data sheet, 2017, https://www.solvay.com/sites/g/files/srpend221/files/2018-10/solvene-T-EAP_EN_0_0.PDF. (Accessed 6 December 2018).
[45] Y.-W. Lu, C.-J. Kim, Microhand for biological applications, Appl. Phys. Lett. 89 (2006) 164101, http://dx.doi.org/10.1063/1.2362602.
[46] C. Richter, H. Lipson, Untethered hovering flapping flight of a 3d-printed mechanical insect, Artif. Life. 17 (2011) 73–86, http://dx.doi.org/10.1162/artl_a_00020.
[47] M. Karásek, F.T. Muijres, C. De Wagter, B.D.W. Remes, G.C.H.E. de Croon, A tailless aerial robotic flapper reveals that flies use torque coupling in rapid banked turns, Science 361 (2018) 1089–1094, http://dx.doi.org/10.1126/science.aat0350.